

# Inclined film boiling: Film stability and heat transfer

Eskil Aursand<sup>a,b,\*</sup>, Stephen H. Davis<sup>b</sup>

<sup>a</sup> Department of Energy and Process Engineering, Norwegian University of Science and Technology (NTNU), Kolbjørn Hejes v. 1B, Trondheim N-7491, Norway

<sup>b</sup> Department of Engineering Sciences and Applied Mathematics, McCormick School of Engineering and Applied Science, Northwestern University, 2145 Sheridan Road, Evanston, IL 60208, United States

---

## Abstract

An inertially modified long-wave model is used to analyze the stability of inclined saturated film boiling. By performing quasi-parallel linear stability analysis on this model and combining the result with a heat-transfer model, an explicit expression for the heat-transfer coefficient is obtained. The results appear to fit all relevant data for film-boiling heat-transfer coefficient within an error of 15%.

**Keywords:** Film boiling, Vapor thin-film, Inertial instabilities, Heat transfer, Inclination angle

---

## 1. Introduction

When a liquid is put in contact with a solid surface that is  $\Delta T$  degrees hotter than the liquid's saturation temperature there is a resulting boiling heat flux  $q$ . The plot of  $q$  vs.  $\Delta T$  is called the *boiling curve*, which was first characterized by Nukiyama (1934). At superheat values ( $\Delta T$ ) beyond the conventional nucleate boiling regime, one finds the *film-boiling* regime (Dhir, 1998). This is characterized by a relatively low heat flux due to the formation of a continuous vapor film between the surface and the liquid, which leads to two issues of practical concern: The limits of the film-boiling regime (Leidenfrost point) and the heat transfer in the film-boiling regime. The present work is concerned with the latter, in the context of saturated natural-convection non-horizontal film boiling.

The heat transfer coefficient (HTC) of vertical/inclined film boiling was first studied by Bromley (1950), and the resulting model has come to be known as the *laminar smooth interface* (LSI) model. The model was later expanded to include liquid drag effects by authors such as Koh (1962) and Kaneyasu and Takehiro (1966), creating the *two-layer models*. These LSI models are based on a steady-state balance between vapor buoyancy and surface/interface drag, while neglecting inertial effects and assuming that evaporation is purely due to conductive heat transfer. The result is that the vapor-film thickness grows as  $h(x) \sim x^{1/4}$ , where  $x$  is the distance along the solid surface starting from the leading edge. Since the heat transfer occurs mainly by conduction across the film, this implies that the local heat flux decreases as  $q(x) \sim x^{-1/4}$  and it

follows that the average HTC of a plate of length  $\ell$  would be

$$\overline{\mathcal{H}}(\ell) = \frac{4k_v}{3h(\ell)} \sim \ell^{-1/4}, \quad (1)$$

with  $k_v$  being the vapor conductivity. However, further research showed that this is only true for very short plates/rods (about  $\ell < 1$  cm). For longer surfaces it has been established that the time-averaged heat flux has practically no dependence on distance from the leading edge. Consequently, the average HTC is independent of total surface length  $\ell$  and severely underpredicted by the smooth interface model (Hsu and Westwater, 1958; Suryanarayana and Merte, 1972; Bui and Dhir, 1985; Nishio and Chandratilleke, 1991; Nishio and Ohtake, 1993; Vijaykumar and Dhir, 1992). It is evident that the liquid-vapor interface profile is unsteady and far from smooth, with waves/crests running in the direction dictated by buoyancy.

These discoveries seemed to imply that the LSI solution has a limit to its stability, in the sense that it may only grow to a certain critical thickness before collapsing and thus yielding an average film thickness smaller than one would expect. This led to the proposal of *laminar vapor-film unit* (LVFU) type models by authors such as Bui and Dhir (1985) and Nishio and Chandratilleke (1991). These models assume that the LSI solution only grows across a certain critical length scale  $\lambda_c$  before collapsing to a near-zero film thickness and giving way to the next identical unit. While these crests will in reality move along the surface, the time-averaged HTC will be close to the corresponding stationary profile. Given these assumptions, the measured time/space averaged HTC for a long plate ( $\ell \gg \lambda_c$ ) would be

$$\mathcal{H} = \overline{\mathcal{H}}(\lambda_c), \quad (2)$$

---

©2018. Made available under the CC-BY-NC-ND 4.0 license. <https://doi.org/10.1016/j.ijmultiphaseflow.2018.11.017>

\*Corresponding author

Email address: [eskil.aursand@ntnu.no](mailto:eskil.aursand@ntnu.no) (Eskil Aursand)

with  $\overline{H}$  given by the LSI solution Eq. (1). Since  $\lambda_c$  is not dependent on the total plate length, this would explain the apparent non-dependence on  $\ell$  in the case of long plates. Thus, in the context of the LVFU model the main challenge is to determine the length scale  $\lambda_c$ , which is essentially an issue of hydrodynamic stability. There have typically been two approaches to determining  $\lambda_c$  in the literature:

- Semi-empirical models: Derive the model based on LSI-type solutions with the critical Reynolds number as an empirical parameter, and fit it to a series of experiments. Make further predictions by assuming that the critical Reynolds number is constant under different conditions (e.g. Kim and Suh (2013)).
- Hybrid models: Apply classical potential-flow stability analysis to investigate the stability of the interface implied by the LSI solution (e.g. Bui and Dhir (1985); Nishio and Chandratilleke (1991); Kolev (1998); Aursand (2018)). Such an analysis generally includes a mixture of Kelvin–Helmholtz and Rayleigh–Taylor effects, depending on plate inclination.

Both of these methods have some issues: The former uses empirical fitting and thus does not provide any insight into why the vapor-film breaks down at a certain Reynolds number. The latter combines potential-flow (irrotational) analysis with a base state from the lubrication approximation that is far from irrotational. Despite this, both methods demonstrate clearly that inertial (Reynolds-number dependent) instabilities are central to the problem. The present work suggests a third method which is able to predict the dominant instabilities of inclined film-boiling based on a set of partial differential equations related to the long-wave approximation methods for thin-film flow. In this way, both the base state and the stability analysis stem from the same formalism, and this avoids the inconsistent addition of potential-flow theory.

The use of long-wave approximation methods to describe the transient dynamics of thin liquid films has a long history, as reviewed by Oron et al. (1997), Myers (1998) and Craster and Matar (2009). Similar use for thin vapor films is somewhat less developed, but the method has been applied to horizontal film boiling by authors such as Panzarella et al. (2000) and Aursand et al. (2018).

The long-wave (lubrication) approximation relies on a film aspect-ratio  $\epsilon$ , which is essentially the ratio between film thickness and disturbance wavelength. Terms of order  $\mathcal{O}(\epsilon^2)$  and  $\mathcal{O}(\epsilon\text{Re})$  are then neglected, which vastly simplifies the Navier–Stokes equation. Simple integration of the continuity equation across the film then allows for the derivation of a highly-nonlinear equation for the film thickness. Crucially, this method does not merely require that  $\epsilon$  is small but also that the Reynolds number ( $\text{Re}$ ) is small enough. This is easily valid for horizontal film boiling, but as shown in Aursand (2018), applying this method to vertical film boiling fails to predict the all-important inertial instability. This is because the strong buoyancy greatly

increases the Reynolds number in the vapor film, and the  $\epsilon\text{Re}$ -terms are no longer negligible.

In Sec. 2 the standard long-wave method is extended by only neglecting terms  $\mathcal{O}(\epsilon^2)$  while retaining the inertial terms  $\mathcal{O}(\epsilon\text{Re})$ . The resulting governing equations and boundary conditions are similar to the ones formulated in Burelbach et al. (1988) and Joo et al. (1991) for horizontal/falling liquid films and more recently in Aursand et al. (2018) for horizontal vapor films, except there are additional  $\mathcal{O}(\epsilon\text{Re})$  inertial terms. These additional terms significantly complicate the momentum equation, and the problem may no longer be reduced to a single equation for the film thickness. Following the Karman–Pohlhausen type integral boundary-layer methods of Alekseenko et al. (1985) and Prokopiou et al. (1991), the momentum equation is integrated across the film while assuming a parabolic velocity profile. As discussed in the reviews Oron et al. (1997, Sec. 6B) and Chang (1994), this inevitably leads to a complicated system of coupled partial differential equations (PDE) in two variables: The film thickness and the vapor flow rate.

In Sec. 3 quasi-parallel linear stability analysis is applied to the model in order to find a complex dispersion relation for harmonic disturbances. This allows the determination of a stability condition for given case-parameters and film thickness. Specifically it allows the determination of the critical Reynolds number for the onset of inertial instabilities and the wavelength of the resulting waves. Predicting the critical Reynolds number within the long-wave formalism is one of the significant novelties of the present work, as it previously has had to be empirically estimated in works such as Kim and Suh (2013). In Sec. 4 the estimated disturbance wavelength  $\lambda_c$  is combined with the LVFU heat-transfer model in Eq. (2) to make a prediction for the long-plate heat-transfer coefficient. This prediction is subsequently compared with experimental data in Sec. 5. Finally, the validity and implications of the findings herein are discussed in Sec. 6, before the conclusions are summarized in Sec. 7.

## 2. Model

### 2.1. Problem description

The physical problem to be considered is that of inclined planar saturated film-boiling, as illustrated in Fig. 1. The problem involves a large heated solid surface submerged in a liquid at an angle  $\alpha$ . A local coordinate system  $(x, z)$  is aligned with the solid surface, and the liquid–vapor interface is located at  $z = h(x, t)$ , with  $t$  being time. The goal is to predict the dynamics of the film-thickness function  $h(x, t)$ , and under what conditions the time-independent solutions are stable.

A case is defined by the (assumed constant) fluid properties, the plate angle  $\alpha$  and the characteristic temperature difference  $\Delta T = T_w - T_s$ , where  $T_w$  is a given solid surface temperature and  $T_s$  is the fluid’s saturation temperature.

The liquid bulk ( $z \gg h$ ) is assumed to be held at the liquid's saturation temperature  $T_s$ .

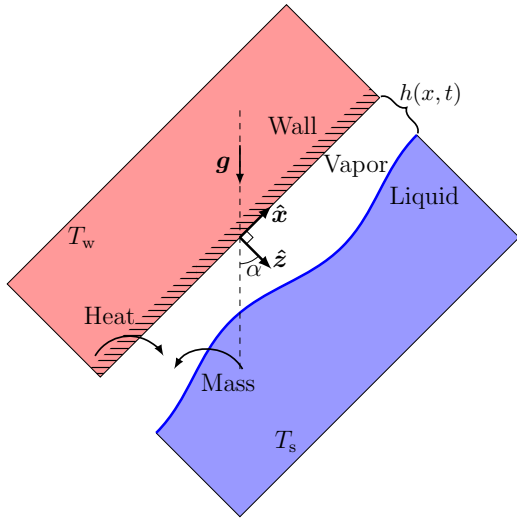


Figure 1: Illustration of the planar film-boiling problem. A wall at angle  $\alpha$  supplies heat to a boiling liquid, which feeds vapor into the vapor film between. Buoyancy then drives vapor flow along the wall. The goal is to predict the dynamics of the film thickness function  $h(x, t)$ .

## 2.2. Long-wave approximation with inertia

### 2.2.1. Governing equations and boundary conditions

The derivation and non-dimensionalization of the governing equations is covered in [Appendix A](#), and only the core principles behind the derivation will be summarized below. The derivation is a generalization of the one in [Aursand et al. \(2018\)](#) for non-horizontal configurations, which in turn was inspired by the work of [Burelbach et al. \(1988\)](#) for evaporating liquid films. The dimensionless variables describing the system are summarized in [Table 1](#).

The expansion parameter in the long-wave approximation is the aspect-ratio of the disturbances,

$$\epsilon = \frac{h_0}{x_0} \ll 1, \quad (3)$$

where  $h_0$  is the typical film thickness and  $x_0 = \lambda/(2\pi)$  is the longitudinal scale given from the disturbance wavelength  $\lambda$ . According to the long-wave approach,  $x_0$  is used as the scale for  $x$ , and  $h_0$  is used as the scale for  $z$  and  $h$ . The velocity scale is set to

$$u_0 = \frac{gh_0^2\Delta\rho}{12\mu_v}, \quad (4)$$

as explained in [Appendix B](#). The tangential velocity  $u$  is scaled with  $u_0$ . Continuity then implies that the normal velocity  $w$  should be scaled by  $w_0 = \epsilon u_0$ . With this choice of  $u_0$  the relevant dimensionless parameters more generally

defined in [Appendix A.3](#) may be written as

$$\begin{aligned} \text{Re} &= \frac{\rho_v \Delta \rho g h_0^3}{12 \mu_v^2} && \text{(Reynolds number)}, \\ E &= \frac{12 \mu_v k_v \Delta T}{\rho_v \Delta \rho g \hat{L} h_0^3} && \text{(Evaporation number)}, \\ \text{Ca} &= \frac{\Delta \rho g h_0^2}{12 \sigma_0} && \text{(Capillary number)}, \\ K &= \frac{\tilde{K} k_v}{h_0 \hat{L}} && \text{(Disequilibrium number)}, \\ M &= \frac{12 \gamma \Delta T}{\Delta \rho g h_0^2} && \text{(Marangoni number)}, \\ S &= \frac{k_v \Delta T}{\mu_v \hat{L}} && \text{(Vapor-thrust number)}, \\ \text{Pr} &= \frac{\mu_v c_{p,v}}{k_v} && \text{(Vapor Prandtl number)}, \\ \Psi &= \mu_v / \mu_l && \text{(Viscosity ratio)}, \\ G_v &= \frac{12 \rho_v}{\Delta \rho} && \text{(Vapor gravity number)}, \\ G_l &= \frac{12 \rho_l}{\Delta \rho} && \text{(Liquid gravity number)}, \\ G &= G_l - G_v = 12 && \text{(Gravity number)}. \end{aligned} \quad (5)$$

Here,  $\rho_v$  is the vapor density,  $\rho_l$  is the liquid density,  $\Delta \rho = \rho_l - \rho_v$ ,  $g$  is the gravitational acceleration,  $\mu_v$  is the vapor viscosity,  $\mu_l$  is the liquid viscosity,  $c_{p,v}$  is the vapor heat capacity,  $k_v$  is the vapor thermal conductivity,  $\hat{L}$  is the effective latent heat of vaporization,  $\tilde{K}$  is a constant from the kinetic theory evaporation model,  $\sigma_0$  is the surface tension at saturation, and  $\gamma$  is the temperature sensitivity of surface tension. The effective latent-heat is used to account for the *sensible-heat effect*. It modifies the conventional latent heat ( $L$ ) according to  $\hat{L} = L + c_{p,v} \Delta T / 2$ , as used in [Bui and Dhir \(1985\)](#). This only has a significant effect for large superheats ( $\Delta T > T_s$ ).

Given these dimensionless numbers and the scaling described in [Appendix A](#), the governing equations may be written as

$$U_X + W_Z = 0, \quad (6)$$

$$\epsilon \text{Re} (U_\tau + U U_X + W U_Z) = -(P + \Phi)_X + U_{ZZ}, \quad (7)$$

$$(P + \Phi)_Z = 0, \quad (8)$$

$$\epsilon \text{Re Pr} (\theta_\tau + U \theta_X + W \theta_Z) = \theta_{ZZ}, \quad (9)$$

where Eq. (6) is the continuity equation, Eqs. (7) and (8) are the momentum equations, and Eq. (9) is the energy equation. Note that a subscript of either  $X$ ,  $Z$  or  $\tau$  implies differentiation with respect to that variable. The body-force potential is given by

$$\Phi = \Phi_0 + G_v (aX + ebZ), \quad (10)$$

where we, as opposed to the more general formulation in [Appendix A.1](#), have neglected the van der Waals interaction term. Here, the parameters  $a$  and  $b$  are simply

Table 1: Overview of dimensionless variables in the governing equations. By default variables describe the vapor, and a subscript “l” indicates the corresponding liquid variable outside the vapor film.

Variable	Description	Scaling	
$X$	Parallel coordinate	$X = x/x_0$	
$Z$	Perpendicular coordinate	$Z = z/h_0$	
$\tau$	Time	$\tau = t/t_0$	$t_0 = x_0/u_0$
$H(X, \tau)$	Film thickness	$H = h/h_0$	
$U(X, Z, \tau)$	Velocity ( $X$ -component)	$U = u/u_0$	
$W(X, Z, \tau)$	Velocity ( $Z$ -component)	$W = w/w_0$	$w_0 = \epsilon u_0$
$P(X, Z, \tau)$	Pressure	$P = p/p_0$	$p_0 = \mu_v u_0 / (\epsilon h_0)$
$\Phi(X, Z, \tau)$	Body-force potential	$\Phi = \phi/p_0$	
$\theta(X, Z, \tau)$	Temperature	$\theta = (T - T_s)/\Delta T$	
$J(X, \tau)$	Evaporation mass flux	$J = j/j_0$	$j_0 = k_v \Delta T / (h_0 L)$
$\theta_i(X, \tau)$	Interface temperature	$\theta_i = (T_i - T_s)/\Delta T$	

shorthands for the inclination effects,  $a = \sin(\alpha)$  and  $b = -\cos(\alpha)$ , respectively. Additionally, the kinetic-theory evaporation model relates the evaporation rate to the interface superheat,

$$KJ = \theta_i. \quad (11)$$

The parameter  $K$  indicates the relative importance of non-equilibrium evaporation effects, with the limit  $K \rightarrow 0$  representing the quasi-equilibrium approximation (interface at saturation). The boundary conditions at the wall are simply no-slip and a given temperature

$$[U]_{Z=0} = [W]_{Z=0} = 0, \quad (12)$$

$$[\theta]_{Z=0} = 1. \quad (13)$$

At the liquid–vapor interface, the standard boundary conditions are

$$[U - U_l]_{Z=H} = 0, \quad (14)$$

$$\epsilon [H_\tau + UH_X - W]_{Z=H} = EJ, \quad (15)$$

$$[P - P_l]_{Z=H} = -\epsilon ESJ^2 - \epsilon^3 \text{Ca}^{-1} H_{XX}, \quad (16)$$

$$[U_Z - \Psi^{-1} U_{l,Z}]_{Z=H} = -\epsilon M [\theta_i]_X, \quad (17)$$

$$-[\theta_Z]_{Z=H} = J \quad (18)$$

where Eq. (14) is the no-slip condition, Eq. (15) is the kinetic boundary condition (with evaporation), Eq. (16) is the normal stress balance, Eq. (17) is the tangential stress balance, and Eq. (18) is the energy balance. Compared to the more general formulation in [Appendix A.1](#), we have neglected the heat transfer between interface and liquid bulk. As shown in [Aursand et al. \(2018\)](#), its effect is very small regardless of film thickness.

In the  $\epsilon \text{Re} \rightarrow 0$  and horizontal limits, the above equations are equivalent to the work in [Burelbach et al. \(1988\)](#) for evaporating liquid thin films, given the necessary adjustments due to the liquid–vapor role reversal. However, due to the fact that the outside bulk phase is now dense compared to the thin film, some additional assumptions are required to still arrive at a closed one-sided model

which avoids having to solve a separate set of PDEs for the liquid dynamics:

- Liquid pressure closure: Assume that the liquid pressure at a given position may be approximated by the hydrostatic pressure corresponding to that position. This provides the unknown  $[P_l]_{Z=H}$  in Eq. (16):

$$[P_l]_{Z=H} = -G_1 (aX + \epsilon bH), \quad (19)$$

- Liquid shear closure: The tangential stress balance Eq. (17) can not initially be used due to the unknown liquid shear  $U_{l,Z}$  at the interface. However, this term vanishes in the hypothetical free-surface case ( $\Psi \rightarrow \infty$ ), and this yields a solvable problem. Since it is known that this case should represent the maximum possible interface velocity due to the absence of liquid drag, one may make the assumption that the actual interface velocity  $[U]_{Z=H}$  is some fraction of this hypothetical maximum value. By introducing the constant factor  $\eta \in [0, 1]$ , which should only depend on fluid properties, the liquid shear closure may formally be expressed as

$$[U]_{Z=H} = \eta \left( \lim_{\Psi \rightarrow \infty} [U]_{Z=H} \right). \quad (20)$$

The above two assumptions are essentially the same as those made for the case of horizontal film-boiling in [Aursand et al. \(2018\)](#). For consistency,  $\eta$  must have the property that

$$\eta \rightarrow \begin{cases} 1 & \Psi \rightarrow \infty \quad (\text{Maximum interface velocity.}) \\ 0 & \Psi \rightarrow 0 \quad (\text{Zero interface velocity.}) \end{cases} \quad (21)$$

In practice, the problem in the free-surface case is solved first, and then Eq. (20) is used to include the effects of liquid drag on the vapor film. As shown in [Appendix C](#), earlier models indicate that  $\eta$  may be estimated from

$$\eta = \frac{3}{16} \left( \frac{\rho_v \mu_v}{\rho_l \mu_l} \right)^{1/4}, \quad (22)$$

which means that  $\eta$  will typically be in the range of 0.01–0.05.

### 2.2.2. General considerations

The following relations derived from the equations in the previous section are valid in both the low-Re and the high-Re cases. First, note that the *reduced pressure*, defined as  $\bar{P} = P + \Phi$ , is independent of  $Z$  according to Eq. (8). This means that for a given  $X$  it may be evaluated at any  $Z$ , and by choosing to evaluate it at  $Z = H$ , one finds that

$$\bar{P}_X(X) = - \underbrace{G(a + \epsilon b H_X)}_{\text{gravity}} - \underbrace{\epsilon^3 \text{Ca}^{-1} H_{XX}}_{\text{capillary}} - \underbrace{\epsilon ES(J^2)}_{\text{vapor thrust}}, \quad (23)$$

which is needed for the right-hand side of Eq. (7). This expression captures not only the conventional gravity and capillary (surface tension) contributions, but also vapor thrust effect due to strong evaporation. Second, one may integrate Eq. (6) across the film while applying Leibniz's integral rule and the boundary conditions Eqs. (12) and (15) to find the general mass-conservation PDE,

$$H_\tau + \left( \int_0^H U dZ \right)_X = \frac{E}{\epsilon} J. \quad (24)$$

Eq. (24) is the sought-after PDE for the film thickness  $H(X, \tau)$ . However, it requires two additional pieces: The velocity profile  $U$  and the evaporation rate  $J$ , both as functions of  $H$ . If it may be assumed that  $\epsilon \text{Re} \ll 1$ , it is relatively simple to proceed, and one retains a single PDE for  $H$ , as shown in Sec. 2.3. If not, it will couple to a second PDE for the mass-flow rate, as shown in Sec. 2.4

## 2.3. The $\epsilon \text{Re} \ll 1$ approximation

### 2.3.1. PDE for film thickness

In the classical lubrication theory, it is assumed that Re is so small that terms  $\mathcal{O}(\epsilon \text{Re})$  may be neglected, which leads to the  $X$ -momentum and energy equations, Eqs. (7) and (9), being vastly simplified. Since  $\bar{P}$  is independent of  $Z$ , the velocity profile may be found by integrating Eq. (7) twice and applying the velocity boundary conditions,

$$U = \frac{1}{2} \bar{P}_X (Z^2 - (1 + \eta)HZ) - \epsilon \eta KM J_X Z. \quad (25)$$

The corresponding mass flow rate is

$$\int_0^H U dZ = -\frac{\xi}{12} \bar{P}_X H^3 - \frac{1}{2} \epsilon \eta KM J_X H^2, \quad (26)$$

with the shorthand  $\xi = 1 + 3\eta$ . Similarly, in this approximation the temperature profile

$$\theta = 1 - \frac{1 - \theta_i}{H} Z \quad (27)$$

satisfies Eq. (9) and the temperature boundary conditions. When combined with the energy balance Eq. (18) and the evaporation model Eq. (11), this leads to the evaporation rate being

$$J = \frac{1}{H + K}. \quad (28)$$

By inserting Eqs. (23), (26) and (28) into Eq. (24), one obtains a nonlinear PDE for  $H(X, \tau)$ ,

$$\begin{aligned} \epsilon H_\tau + \frac{\xi G}{12} \epsilon [H^3 (a + \epsilon b H_X)]_X \\ - \frac{\xi ES}{6} \epsilon^2 \left[ \left( \frac{H}{H + K} \right)^3 H_X \right]_X + \frac{\xi}{12 \text{Ca}} \epsilon^4 [H^3 H_{XXX}]_X \\ + \frac{1}{2} \epsilon^2 \eta KM \left[ \left( \frac{H}{H + K} \right)^2 H_X \right]_X = E \frac{1}{H + K}. \end{aligned} \quad (29)$$

Eq. (29) is a generalization of Aursand et al. (2018, Eq. 2.66) from horizontal film boiling to arbitrary orientation. However, as will be shown, this equation does not capture the essential inertial instabilities arising in non-horizontal film boiling.

### 2.3.2. Approximate steady-state solution

The steady state is expected to have a very smooth interface, which would imply a very small  $\epsilon$ . If one keeps only first order  $\epsilon$ -terms from Eq. (29), set the time-derivative to zero, and assume that the film has grown so thick that  $K \ll H$ , the following ODE is found for the steady-state solution  $\bar{H}(X)$ ,

$$\epsilon \bar{H}_X = \frac{4E}{\xi G a} \frac{1}{\bar{H}^3}. \quad (30)$$

With the assumption that  $H = 0$  at the leading edge  $X = 0$ , Eq. (30) may be integrated to find the explicit expression

$$\bar{H}(X) = \left( \frac{16E}{\epsilon \xi G a} X \right)^{1/4}. \quad (31)$$

The corresponding dimensional form is

$$\bar{h}(x) = \left( \frac{16 \mu_\nu k_\nu \Delta T}{\xi a \rho_\nu \Delta \rho g \hat{L}} x \right)^{1/4}, \quad (32)$$

which reveals that this is the common LSI-type solution introduced in Sec. 1. This solution will be used to approximate the actual steady state in the following stability analysis.

Let the film thickness scale  $h_0$  be given by the steady solution Eq. (32) in the vertical case. The Reynolds number as given by Eq. (5) then grows as  $\text{Re} \sim x^{3/4}$ , and thus, it will eventually grow too large for the  $\epsilon \text{Re} \ll 1$  approximation. However, a longer distance from the leading edge will also accommodate longer disturbance waves, i.e. a smaller  $\epsilon$ . If the longest disturbance wavelength that

fits is equal to  $x$ , the distance from the leading edge, the smallest allowed  $\epsilon$  is  $\bar{\epsilon} = h_0(x)/x$ . The product of this and  $\text{Re}$  is surprisingly simple,

$$\bar{\epsilon}\text{Re} = \frac{4 k_v \Delta T}{3 \xi \mu_v \hat{L}} = \frac{4 S}{3 \xi} \sim \mathcal{O}(10^{-1}). \quad (33)$$

Since  $\epsilon > \bar{\epsilon}$ , this is actually a lower bound for  $\epsilon\text{Re}$ , and thus, one must conclude that no allowed disturbance to the steady state may actually satisfy  $\epsilon\text{Re} \ll 1$ .

The above does not imply that  $\epsilon\text{Re} \ll 1$  is invalid in the commonly studied case of horizontal film-boiling since the velocity scale in Eq. (4) is not appropriate in such cases. However, for the purposes of non-horizontal film-boiling, the inertial  $\epsilon\text{Re}$  terms must be retained. The next section shows how.

#### 2.4. $\epsilon\text{Re} \sim \mathcal{O}(1)$

##### 2.4.1. Averaged momentum equation

If one integrates the  $X$ -momentum equation, Eq. (7), across the layer while applying the continuity equation, Eq. (6), the wall boundary condition, Eq. (12), and the kinetic boundary condition, Eq. (15), the result is

$$\begin{aligned} \epsilon\text{Re} \left( \left[ \int_0^H U dZ \right]_\tau + \left[ \int_0^H U^2 dZ \right]_X - \frac{E}{\epsilon} [U]_{Z=H} J \right) \\ = -\bar{P}_X H + [U_Z]_{Z=H} - [U_Z]_{Z=0}. \end{aligned} \quad (34)$$

This result is similar to the one on liquid films by [Alekseenko et al. \(1985, Eq. 15\)](#), except that Eq. (34) is complicated by the inclusion of evaporation, interface drag (not a free surface), and a driving force  $\bar{P}_X$  that includes vapor thrust and vdW forces in addition to gravity and surface tension.

The left-hand side of Eq. (34) constitutes the inertia correction, and this would be zero in the conventional lubrication approximation. In order to evaluate the integrals in Eq. (34) and obtain a PDE for scalar quantities, it is necessary to model the velocity profile  $U(Z)$ . This is done in the next section.

##### 2.4.2. Assumed velocity profile

In Sec. 2.3 it was shown how the low-Re case leads to a parabolic velocity profile Eq. (25) that is zero at the wall and small but non-zero at the interface. It is now assumed that the general velocity-profile has the same shape, and this will be used to compute the inertial corrections at higher Re. Such a generic profile may be written as

$$U(X, Z) = \hat{U}(X) \left[ (1 + s(X)) \frac{Z}{H} - \left( \frac{Z}{H} \right)^2 \right], \quad (35)$$

where the overall flow-speed is given by the function  $\hat{U}(X)$ , and the relative speed at the interface is given by the function  $s(X) \ll 1$ . The boundary conditions Eqs. (17)

and (20) provide a solution for  $s$  in terms of  $\eta$  and the thermocapillary effect,

$$s(X) = \eta \left( 1 - \epsilon K M \frac{H J_X}{\hat{U}} \right) \quad (36)$$

where the evaporation model Eq. (11) has been used to represent the interface temperature in terms of  $J$ . By then defining a flow rate function  $Q$ ,

$$Q = \frac{\xi}{6} H \hat{U}, \quad (37)$$

and some short-hand functions of  $\eta$ ,

$$\xi = 1 + 3\eta, \quad (38)$$

$$\zeta = \frac{10\eta^2 + 5\eta + 1}{\xi^2} = 1 - \eta + \mathcal{O}(\eta^2), \quad (39)$$

$$\chi = \frac{\xi + \eta}{\xi} = 1 + \eta + \mathcal{O}(\eta^2), \quad (40)$$

the integrals needed in Eq. (34) may be calculated as

$$\int_0^H U dZ = Q - \frac{1}{2} \epsilon \eta K M H^2 J_X, \quad (41)$$

$$\begin{aligned} \int_0^H U^2 dZ = \frac{6}{5} \zeta \frac{Q^2}{H} - \chi K \epsilon \eta M H Q J_X \\ + \frac{1}{3} (K \epsilon \eta M)^2 H^3 (J_X)^2, \end{aligned} \quad (42)$$

and the right-hand side friction term as

$$[U_Z]_{Z=H} - [U_Z]_{Z=0} = -\frac{12}{\xi} \frac{Q}{H^2}. \quad (43)$$

The vapor film dynamics are now described by two functions in  $1 + 1$  dimensions:  $H(X, \tau)$  for the film thickness and  $Q(X, \tau)$  for the volumetric flow rate. As will be shown in the next section, the integrated continuity-equation Eq. (24) and the integrated momentum-equation Eq. (34) provide two coupled PDEs for these functions.

##### 2.4.3. Coupled PDEs governing film behavior

It is assumed that the most important inertial corrections happen through the momentum equation, not the energy equation. This means that Eq. (28) is also used as a model for the evaporation mass flux  $J$  in the general case. The thermocapillary effect scales with the overall strength of evaporation and thus, the film thickness. Its relative strength is indicated by the film-thickness independent constant  $\hat{M}$ , defined as

$$\hat{M} = \frac{K M}{E} = \frac{\rho_v \gamma \tilde{K}}{\mu_v}. \quad (44)$$

Then, it is assumed that

$$E \ll 1, \quad K \ll 1, \quad , \quad (45)$$

so that terms  $\mathcal{O}(E^2)$ ,  $\mathcal{O}(K^2)$  and  $\mathcal{O}(EK)$  may be neglected. This greatly simplifies governing equations and will be justified in the next section. One may now insert Eqs. (28) and (41) into the integrated continuity-equation Eq. (24) to yield the first PDE,

$$\underbrace{\epsilon H_\tau + \epsilon Q_X}_{\text{mass advection}} + \underbrace{\frac{1}{2}\eta E \hat{M} \epsilon^2 H_{XX}}_{\text{thermocapillary}} = \underbrace{E \frac{1}{H}}_{\text{evap.}}. \quad (46)$$

Similarly, one may combine Eqs. (28), (36), (41) and (42) with the integrated momentum-equation Eq. (34) to yield the second PDE,

$$\epsilon \text{Re} \left( \underbrace{Q_\tau + \frac{6\zeta}{5} \left[ \frac{Q^2}{H} \right]_X}_{\text{advection}} + \underbrace{\eta E \hat{M} \left[ \frac{1}{2} \epsilon H_{X\tau} + \chi \epsilon \left[ \frac{Q}{H} H_X \right]_X \right]}_{\text{thermocapillary}} \right) - \underbrace{\frac{E 6\eta}{\epsilon} \frac{Q}{\xi H^2}}_{\text{mom. injection}} = \underbrace{-\bar{P}_X H - \frac{12}{\xi} \frac{Q}{H^2}}_{\text{friction balance}}. \quad (47)$$

with Eq. (23) reduced to

$$\bar{P}_X = - \underbrace{G(a + b\epsilon H_X)}_{\text{gravity}} + \underbrace{2SE\epsilon \frac{H_X}{H^3}}_{\text{vapor thrust}} - \underbrace{\text{Ca}^{-1} \epsilon^3 H_{XX}}_{\text{capillary}} \quad (48)$$

The inertia correction is the left-hand side of Eq. (47). Note also how all non-equilibrium evaporation effects ( $K$ -terms) are negligible under the approximation Eq. (45), except for their part in the thermocapillary effect, which is collected into the parameter  $\hat{M}$ .

Eqs. (46) and (47) with Eq. (48) constitute the main result of this section, and the following content concerns the conditions under which they allow for a stable steady-state solution.

### 2.5. Magnitudes of dimensionless constants

According to Eqs. (46) to (48), the dynamics of the unknown variables  $H$  and  $Q$  at a given inclination are governed by the following dimensionless numbers:

- Re: Strength of inertial effects.
- $E$ : Strength of evaporation effects.
- $\text{Ca}^{-1}$ : Strength of surface tension.
- $\hat{M}$ : Strength of thermocapillary effect relative to evaporation effects.
- $S$ : Strength of vapor thrust effect relative to evaporation effects.
- $\eta$ : Fraction of actual interface velocity to the hypothetical maximum.

The latter three ( $\hat{M}$ ,  $S$  and  $\eta$ ) are only dependent on fluid properties and  $\Delta T$ , and will in most cases be

$$\hat{M} \sim \mathcal{O}(1), \quad S \sim \mathcal{O}(10^{-1}), \quad \eta \sim \mathcal{O}(10^{-2}), \quad (49)$$

Whereas the governing equations depend on  $G$  as well, one sees from Eq. (5) that with the chosen velocity scale it is simply constant and equal to 12. The first four dimensionless numbers in the list are dependent on film-thickness scale  $h_0$ . Fig. 2 shows these four parameters, as well as  $K$ , as functions of  $h_0$ . It indicates that the present approximation, Eq. (45), can be expected to be valid in the region where  $h_0 > 100 \mu\text{m}$ . The following stability analysis will apply to this regime (shaded in Fig. 2).

## 3. Quasi-parallel stability analysis

### 3.1. Base state

The task now is to examine under which conditions stable steady-state solutions to the governing equations Eqs. (46) and (47) exist. This *base state* is denoted by functions  $\bar{H}(X)$  and  $\bar{Q}(X)$  corresponding to  $H$  and  $Q$ , respectively. While these functions are generally not known analytically, when explicit expressions are required they will be approximated by the low-Re solution in Eq. (31). Under the same approximation, the momentum equation tells us that the base state flow rate  $\bar{Q}$  is

$$\bar{Q} = \frac{\xi G a}{12} \bar{H}^3. \quad (50)$$

The stability analysis that will follow is applied locally at a specific position  $X_0$ , and at that point the base state is used to define the film thickness scale  $h_0$ . In order to have an orientation-independent scale, it is defined such that  $\bar{H}(X_0) = 1$  in the vertical configuration, and thus, Eq. (31) implies that

$$\bar{H}(X_0) = a^{-1/4}. \quad (51)$$

### 3.2. Quasi-parallel perturbation analysis

The disturbances  $\hat{H}$  and  $\hat{Q}$  are defined by

$$H(X, \tau) = \bar{H}(X) + c\hat{H}(X, \tau), \quad (52)$$

$$Q(X, \tau) = \bar{Q}(X) + c\hat{Q}(X, \tau), \quad (53)$$

and this combined solution is inserted into the nonlinear governing equations Eqs. (46) and (47). By approximating to first order in the perturbation magnitude,  $\mathcal{O}(c^1)$ , and subtracting the zeroth order (steady state) equations, one arrives at a set of two linear and homogeneous PDEs for the perturbations  $\hat{H}$  and  $\hat{Q}$ . However, a complication arises due to the fact that the coefficients of these linear PDEs depend on  $\bar{H}(X)$ ,  $\bar{Q}(X)$ , and their derivatives. This means that the coefficients are  $X$ -dependent, and standard normal-mode analysis would not apply for the  $X$ -dimension.

This situation may be remedied (in approximation) by applying quasi-parallel analysis. This entails assuming that the base state  $\bar{H}(X)$  is locally constant for the purposes of the stability analysis. This procedure yields PDEs for the perturbations  $\hat{H}$  and  $\hat{Q}$  that formally have

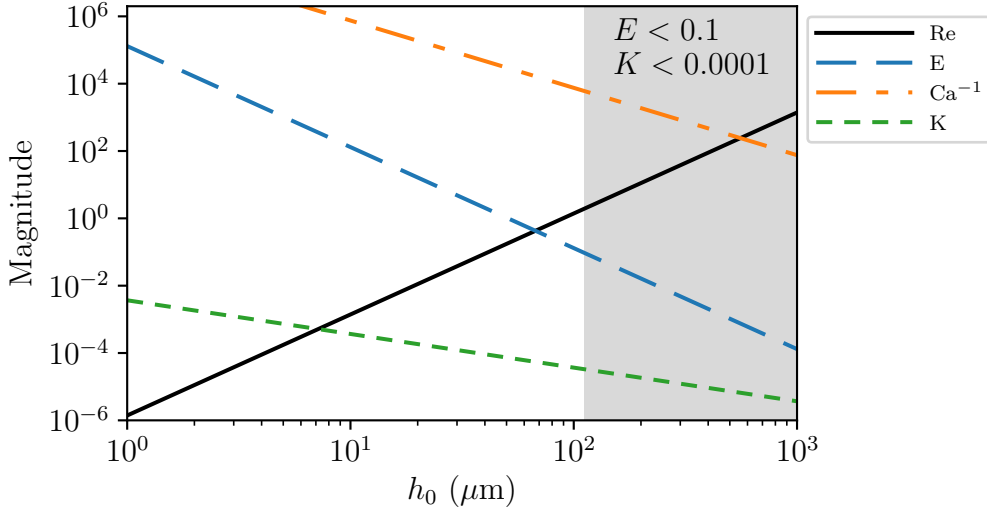


Figure 2: Magnitude of  $h_0$ -dependent dimensionless numbers. This example is made from water boiling at  $\Delta T = 200$  K. The shading marks the region of model validity, i.e. where  $h_0$  is such that both  $E$  and  $K$  are small.

constant coefficients, though the value of these coefficients will depend on the film thickness at which stability is examined. The quasi-constant film thickness at the location under consideration is denoted as  $H_0$ , and due to the choice of scaling, it depends on orientation according to  $H_0 = a^{-1/4}$ . Note that since  $H_0$  is defined as such, the effect of position  $X$  on the stability analysis enters through changes in the film thickness scale  $h_0$ , which in turn affect the dimensionless parameters shown in Fig. 2.

Since the equations for the perturbations now are linear, homogeneous, and with constant coefficients, an arbitrary disturbance may be represented by a linear combination of normal-modes such as the following,

$$\hat{H} = \tilde{H} \exp\left(i \frac{kX - \omega\tau}{\epsilon}\right), \quad \hat{Q} = \tilde{Q} \exp\left(i \frac{kX - \omega\tau}{\epsilon}\right). \quad (54)$$

The division by  $\epsilon$  in the exponent simply means that the dimensionless wavenumber  $k$  and frequency  $\omega$  are defined according to the spatial and temporal scales  $h_0$  and  $h_0/u_0$ , respectively. The long-wave approximation then implies that  $k$  must be small. The following task is to examine temporal stability, which means considering the real wavenumber  $k$  as an input and observing the effect on the resulting complex frequency  $\omega$ . A positive imaginary part of  $\omega$  implies an exponentially growing instability.

### 3.3. General solution

When performing the above described quasi-parallel stability analysis on the governing equations Eqs. (46) and (47), the result is a quadratic equation for  $\omega(k)$ ,

$$c_2\omega^2 + c_1\omega + c_0 = 0 \quad (55)$$

with complex coefficients

$$c_2 = \text{Re}, \quad (56)$$

$$c_1 = \frac{12i}{H_0^2\xi} + \text{Re} \left( \frac{iE}{H_0^2} \left[ 1 - \frac{6\eta}{\xi} \right] - \frac{GaH_0^2\xi\zeta}{5} k \right), \quad (57)$$

$$\begin{aligned} c_0 = & H_0 G b k^2 - 3i G a k - \frac{H_0}{\text{Ca}} k^4 \\ & + \frac{12E}{\xi} \left( \frac{\hat{M}\eta}{2H_0^2} k^2 - \frac{\xi S}{6H_0^2} k^2 - \frac{1}{H_0^4} \right) \\ & + \text{Re} \left( \frac{H_0^4 \zeta G^2 a^2 \xi^2}{120} k^2 + i E G H_0^2 \hat{M} a \eta \xi \left[ \frac{\zeta}{10} - \frac{\chi}{12} \right] k^3 \right. \\ & \left. - \frac{i E G a \xi \zeta}{5} k \right). \end{aligned} \quad (58)$$

While Eq. (55) may be solved directly, the resulting expression does not allow for easy inspection of qualitative effects. Its general behavior must be revealed by repeated numerical solutions.

### 3.4. Low Reynolds number limit

In the limit of negligible inertial effect ( $\text{Re} \rightarrow 0$ ), just like in the classical lubrication approximation, Eq. (55) is simplified to a first-order equation that may be solved explicitly for the complex frequency, here labeled as  $\omega_0$ . The imaginary part turns out to be

$$\begin{aligned} \mathcal{I}(\omega_0) = & - \underbrace{\frac{H_0^3 \xi}{12 \text{Ca}} k^4}_{\text{capillary}} - \underbrace{\frac{\xi E S}{6}}_{\text{Vapor thrust}} k^2 + \underbrace{\frac{\eta E \hat{M}}{2}}_{\text{Thermocap.}} k^2 \\ & + \underbrace{\frac{G b \xi H_0^3}{12}}_{\text{Gravity}} k^2 - \underbrace{\frac{E}{H_0^2}}_{\text{Evap.}}. \end{aligned} \quad (59)$$

This result, while missing the essential inertial effect, is still useful. From Eq. (59) it is clear that the system is

stable at  $k \rightarrow \infty$  by capillarity and as  $k \rightarrow 0$  by evaporation. At intermediate wavenumbers, stability is a matter of balance between the  $k^2$  terms: a stabilizing vapor thrust, a destabilizing thermocapillary effect, and a gravitational (Rayleigh–Taylor) effect, whose sign depends on inclination.

An important note about Eq. (59) is that in the vertical case the only destabilizing influence is thermocapillarity, which is unable to explain the instabilities seen in experiments on vertical plates. The missing piece is the inertial (Kelvin–Helmholtz) instabilities, and these are captured when using the full coefficients in Sec. 3.3.

### 3.5. Limits of stability: Critical Reynolds number

The goal is to evaluate stability as a function of film-thickness scale  $h_0$ . As found in Sec. 3.2, the stability analysis depends on a number of dimensionless parameters, some of which are  $h_0$ -dependent:

$$\text{Re} \propto h_0^3, \quad E \propto h_0^{-3}, \quad \text{Ca} \propto h_0^2. \quad (60)$$

It is convenient to isolate the  $h_0$ -dependence into a single parameter. Here, this is achieved by choosing  $\text{Re}$  as that parameter and letting  $E$  and  $\text{Ca}$  be functions of  $\text{Re}$  through some  $h_0$ -independent relations. These relations are

$$E(\text{Re}) = \frac{S}{\text{Re}}, \quad \text{Ca}(\text{Re}) = \frac{\text{Re}^{2/3}}{B}, \quad (61)$$

where the  $h_0$ -independent parameters  $S$  and  $B$  are defined by Eq. (5) and

$$B = \text{Ca}^{-1} \text{Re}^{2/3} = 12\sigma_0 \left( \frac{\rho_v^2}{144\Delta\rho g \mu_v^4} \right)^{1/3} \sim \mathcal{O}(10^4), \quad (62)$$

respectively. This has the convenient effect that for a given case (fluid,  $\Delta T$  and inclination) stability may be evaluated as a function of the Reynolds number alone.

Since the dispersion relation Eq. (55) is a quadratic equation, it will generally yield two values of  $\omega$  for every given value of  $k$ ; call these  $\omega_+$  and  $\omega_-$ . The typical shapes of these two branches in the vertical case are shown in Fig. 3. It is generally the case that the  $\omega_-$  branch has no potential for instability, and from now on, the interesting branch  $\omega_+$  will simply be labeled as  $\omega$ . Fig. 3 reveals that while the system is stable at both wavenumber extremes, there is a potential for instability at intermediate wavenumbers. that is almost completely due to inertial (Kelvin–Helmholtz type) instabilities. Note also how the low- $\text{Re}$  model ( $\omega_0$ ) fails at predicting this instability.

A plot like Fig. 3 can be made for a range of  $\text{Re}$  values, and this allows the construction of neutral-curve plots, such as in Fig. 4. The neutral curve also indicates the critical Reynolds number and wavenumber, formally defined by:

**Definition.** *The critical Reynolds number ( $\text{Re}_c$ ) is the smallest Reynolds number ( $\text{Re}$ ) for which  $\mathcal{I}(\omega(k)) = 0$  for some value of  $k$ . The corresponding value of  $k$  is the critical wavenumber ( $k_c$ ).*

These two properties,  $\text{Re}_c$  and  $k_c$ , are the most important results from the stability analysis. Their values depend on  $S$ ,  $B$ ,  $\hat{M}$ ,  $\alpha$  and  $\eta$ , though in practice it is found that the thermocapillary effect ( $\hat{M}$ -terms) is too weak to matter in the regime where the present approximation ( $E \ll 1$ ) applies. In contrast, the parameters  $S \propto \Delta T$  and  $B \propto \sigma_0$  both have appreciable effects and may vary much between cases. Their typical ranges for real cases are  $S \in (0.1, 1.0)$  and  $B \in (5000, 30000)$ . Throughout this range it is found that the critical wavenumber  $k_c$ , and thus  $\epsilon$ , is approximately 0.1 or less. This justifies the neglect of terms  $\epsilon^2$  in the long-wave approximation.

Generally, it is necessary to solve iteratively for  $\text{Re}_c$  and  $k_c$  in each case. However, in the vertical case it was discovered through inspection of numerous numerical solutions that the results may be captured to good approximation by the relations

$$\text{Re}_{c\perp} \approx \frac{3}{2} (SB)^{1/4}, \quad (63)$$

$$k_{c\perp} \approx \frac{3}{2} \left( \frac{S}{B} \right)^{1/4}, \quad (64)$$

where the subscript  $\perp$  implies vertical configuration. Given the typical ranges of  $S$  and  $B$ , Eqs. (63) and (64) imply that  $\text{Re}_{c\perp} \in (5, 20)$  and  $k_{c\perp} \in (0.05, 0.2)$ . For non-vertical configurations the results are too complicated to be captured in simple power-laws.

The base state Eq. (32) has a monotonically growing film thickness and thus a monotonically growing Reynolds number, which eventually crosses the critical value  $\text{Re}_c$ . The resulting disturbance is predicted to have the dimensionless wavenumber  $k_c$ , and the corresponding dimensional wavelength is

$$\lambda_c = \frac{2\pi}{k_c} h_0(\text{Re}_c) = \frac{2\pi}{k_c} \left( \frac{12\mu_v^2}{\rho_v \Delta\rho g} \text{Re}_c \right)^{1/3} = \frac{2\pi \text{Re}_c^{1/3}}{k_c} \lambda_0, \quad (65)$$

with the definition

$$\lambda_0 = \left( \frac{12\mu_v^2}{\rho_v \Delta\rho g} \right)^{1/3}. \quad (66)$$

The fluid-dependent length scale  $\lambda_0$  is usually in the range of 10–100  $\mu\text{m}$ . In the vertical case, one may insert Eqs. (63) and (64) into Eq. (70) to find the expression

$$\lambda_{c\perp} = 2\pi \left( \frac{2}{3} \right)^{2/3} \underbrace{\left( \frac{B^2}{S} \right)^{1/6}}_{\sim \mathcal{O}(10)} \lambda_0, \quad (67)$$

i.e. the critical wavelength will be about 100 times longer than  $\lambda_0$ .

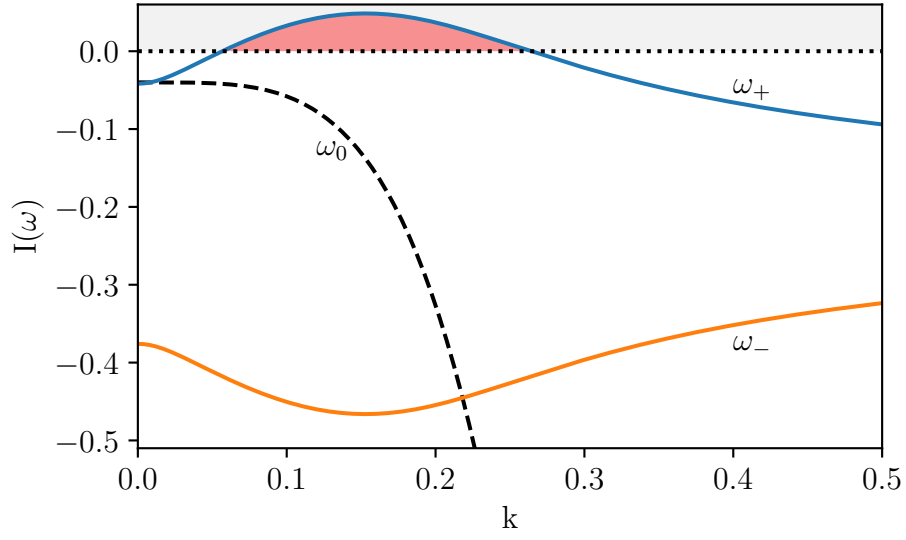


Figure 3: Imaginary part of typical solutions of Eq. (55) ( $\omega_+, \omega_-$ ) and Eq. (59) ( $\omega_0$ ) as functions of dimensionless wavenumber  $k$ , for the vertical case ( $\alpha = \pi/2$ ). Red shading marks the region where  $\mathcal{I}(\omega) > 0$ , i.e. predicted instabilities. This example is made based on  $Re = 25$ ,  $S = 1$ ,  $\hat{M} = 1$ ,  $B = 15000$  and  $\eta = 0.025$ .

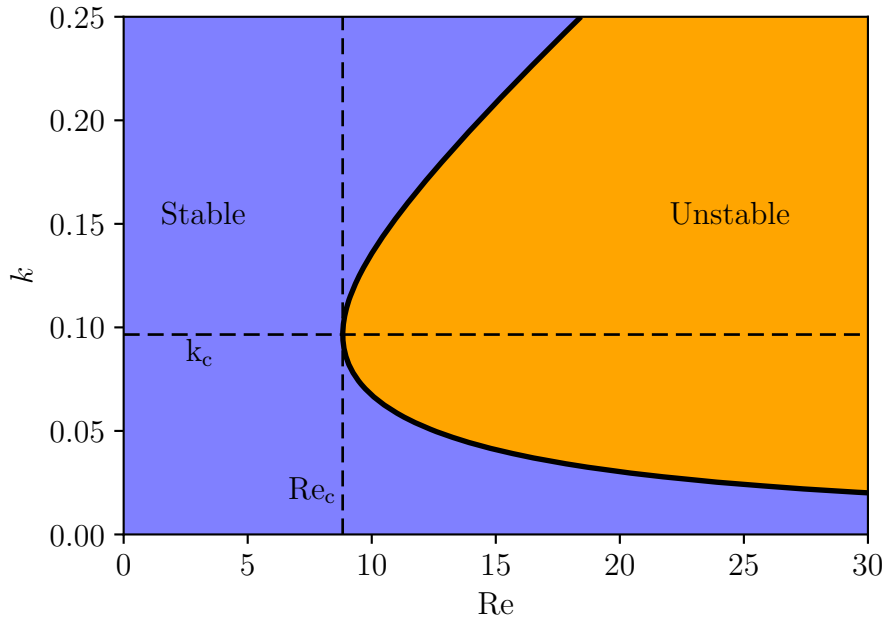


Figure 4: Example of a neutral curve in  $(Re, k)$  space. This plot was generated with parameters corresponding to vertical water film boiling at  $\Delta T = 200$  K. The dashed vertical line shows the critical Reynolds number, and the dashed horizontal line shows the corresponding critical wavenumber.

#### 4. Predicting the long-plate heat-transfer coefficient

Now that a model for the loss of stability has been found, this may be combined with the laminar vapor-film unit (LVFU) model to predict the heat-transfer coefficient (HTC). Given the LVFU model, Eq. (2), the HTC may be found as

$$\mathcal{H} = \frac{4k_v}{3\bar{h}(\lambda_c)} = \mathcal{H}_0 \text{Nu}, \quad (68)$$

with the function  $\bar{h}(x)$  according to Eq. (32). The last equality shows how this may be split into a reference HTC ( $\mathcal{H}_0$ ) and a Nusselt number (Nu). The reference HTC is commonly defined simply as the conductivity divided by some known thickness. However, the present case presents the problem that there is no obvious ab initio known length scale. The only emergent easily calculable length scale so far is  $\lambda_0$ , so here we choose to define  $\mathcal{H}_0$  as the conductive heat transfer across a uniform vapor film of thickness  $\bar{h}(\lambda_0)$ ,

$$\mathcal{H}_0 = \frac{k_v}{\bar{h}(\lambda_0)} = k_v \left( \frac{\xi a \rho_v \Delta \rho g \hat{L}}{16 \mu_v k_v \Delta T \lambda_0} \right)^{1/4}. \quad (69)$$

This definition has the advantage of letting  $\mathcal{H}_0$  be calculable from known case/fluid properties alone, and thus independent of the specific solution of the stability problem. Of course, there are many possible definitions with this property, but this one allows for  $\text{Nu} \sim \mathcal{O}(1)$ . Given the choice of Eq. (69), the Nusselt number is

$$\text{Nu} = \frac{\mathcal{H}}{\mathcal{H}_0} = \frac{4}{3} \left( \frac{\lambda_0}{\lambda_c} \right)^{1/4} = \frac{4}{3} \left( \frac{k_c}{2\pi \text{Re}_c^{1/3}} \right)^{1/4}. \quad (70)$$

Here, Eq. (65) has been used for the critical wavelength. In the general case, one must solve numerically for  $\text{Re}_c$  and  $k_c$  using Eq. (55) and insert the result into Eq. (70). However, as shown earlier, in the vertical case one may use the fitted power laws Eqs. (63) and (64), and this gives

$$\text{Nu}_\perp = \underbrace{\frac{4}{3} \left( \frac{3}{2} \right)^{1/6} \left( \frac{1}{2\pi} \right)^{1/4}}_{=0.9010\dots} \underbrace{\left( \frac{S}{B^2} \right)^{1/24}}_{\sim 0.4 - 0.5}. \quad (71)$$

This reveals a very weak dependence on  $S$  and  $B$ , making the Nusselt number nearly constant/universal. The Nusselt number has been calculated from Eq. (70) for many combinations of  $S$  and  $B$  and plotted against the single parameter  $S/B^2$  in Fig. 5. This plot illustrates how Eq. (71) is a good approximation to the full calculation in the vertical case. It also reveals that Nu follows the  $(S/B^2)^{1/24}$  dependency in non-vertical inclinations as well. However, its reduction when deviating from the vertical configuration is asymmetric. The reason for the asymmetry is that the gravitational (Rayleigh–Taylor) effect is a stabilizing

influence on one side and a destabilizing influence on the other.

The inclination dependence of  $\text{Re}_c$  and  $k_c$  from solving the full model is too complicated to be well estimated by simple power laws such as Eqs. (63) and (64), and thus, an accurate expression like Eq. (71) could not be derived for the general case. However, numerical computations of the resulting Nusselt number with the use of Eq. (70) for a wide variety of  $S$  and  $B$  showed that on the liquid-below-vapor side the Nusselt number may to a decent approximation be given by

$$\text{Nu} \approx a^{1/6} \text{Nu}_\perp, \quad (\text{for } \alpha \leq \pi/2). \quad (72)$$

Note that for the total HTC this  $a^{1/6}$  dependence combines with the  $a^{1/4}$  dependence of  $\mathcal{H}_0$  in Eq. (69), giving a total inclination dependence of  $a^{5/12}$ .

#### 5. Experimental validation

The predictions for the HTC described in Sec. 4 may now be tested against experimental data. Relevant experiments are long-plate film-boiling heat-transfer measurements with a liquid bulk that is stationary and saturated. Note that when making predictions using the model it is crucial to evaluate the vapor properties  $\mu_v$ ,  $\rho_v$ ,  $k_v$  and  $c_{p,v}$  at some average *film-temperature*, not simply at  $T_s$ . In the present work, the common choice of  $T_s + \Delta T/2$  is made for the film temperature. The liquid properties are simply evaluated at the saturation temperature.

Series of HTC measurements on vertical plates under different values of  $\Delta T$  for a variety of fluids were found in the works of Bui and Dhir (1985); Okkonen et al. (1996); Vijaykumar and Dhir (1992); Nishio and Chandratilleke (1991); Hsu and Westwater (1958); Nishio and Chandratilleke (1989); Liaw and Dhir (1986). Given an orientation and a specific fluid, the only remaining variable is the surface superheat  $\Delta T$ . The HTC data are plotted against relative superheat ( $\Delta T/T_s$ ) in Fig. 6. For each fluid, three model curves are shown. They all use Eq. (68) but with different methods for finding Nu: The result from numerically solving for  $\text{Re}_c$  and  $k_c$  and inserting these into Eq. (70), the result from using the simplified model for vertical Nusselt number in Eq. (71), and the result from using a constant  $\text{Nu} = 0.4$ . It is revealed that the full model predicts virtually all the data within a 15% HTC uncertainty and that the simplification in Eq. (71) gives almost identical results.

By dividing the measured HTC by the corresponding  $\mathcal{H}_0$ , one may also find the Nusselt numbers of the data. In Fig. 7 these are compared to the dependence on  $S/B^2$  implied by Eq. (71). This confirms that the Nusselt number is nearly constant/universal and that the weak variations are according to  $(S/B^2)^{1/24}$  is as predicted.

A series of HTC measurements with water on a plate of varying inclinations was provided by Kim and Suh (2013). The inclination-dependence of the HTC is compared with

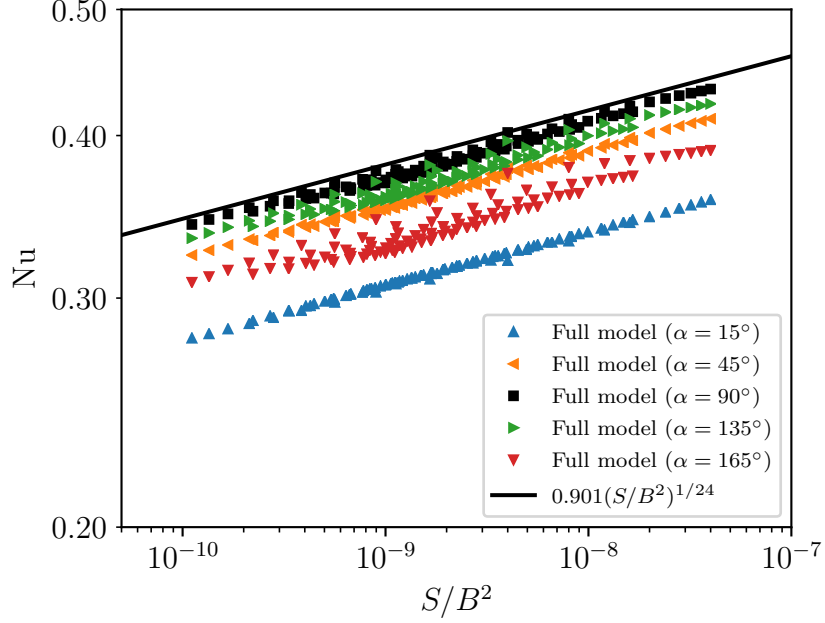


Figure 5: Calculation of the Nusselt number according to Eq. (70) throughout the range  $S \in (0.1, 1.0)$ ,  $B \in (5000, 30000)$ , plotted as a function of  $S/B^2$ . This is repeated for a number of different inclination angles  $\alpha$ . Also shown is the vertical approximation according to Eq. (71).

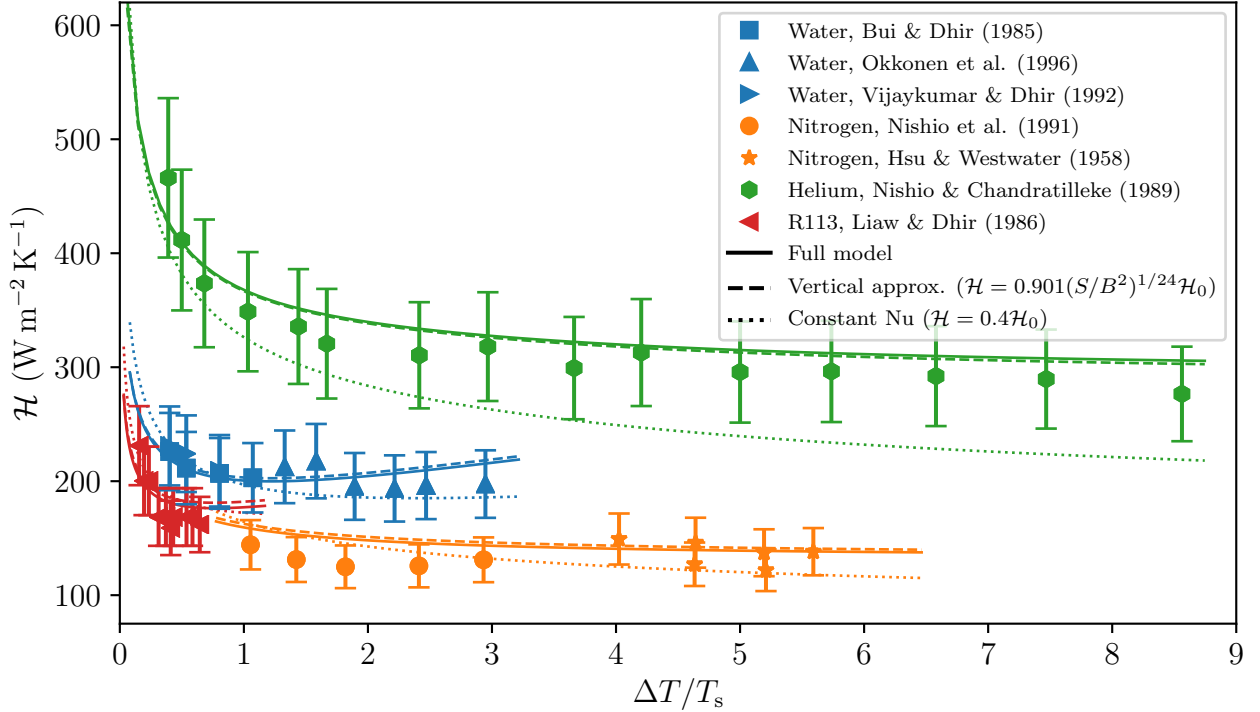


Figure 6: Experimentally measured vertical-plate heat-transfer coefficients plotted against relative surface superheat, with error bars representing a 15% uncertainty. The corresponding model predictions are shown as three lines for each fluid, corresponding to three different models/values for the Nusselt number.

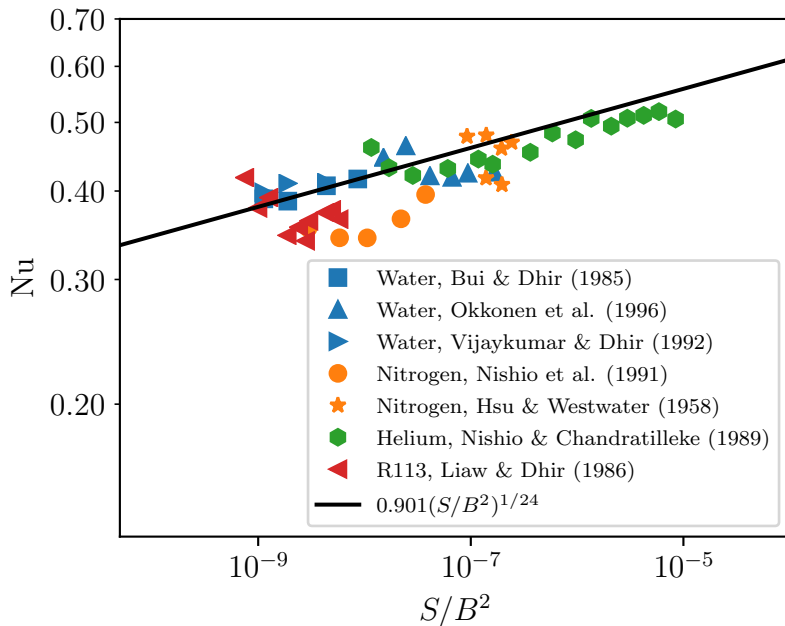


Figure 7: The Nusselt numbers  $Nu = \mathcal{H}/\mathcal{H}_0$  corresponding to the data points in Fig. 6, plotted against  $S/B^2$ . The solid line shows the prediction by Eq. (71).

the predictions of the present model in Fig. 8. Both the full model (numerical solution), and the approximation implied by the combined angular dependence of Eq. (69) and Eq. (72), are shown. As expected, the two are practically identical in the  $\alpha \leq \pi/2$  region, but the approximation does not capture the asymmetry in  $Nu$  and thus, fails slightly in the  $\alpha > \pi/2$  region. For comparison, the  $a^{1/4}$  dependence of the LSI-type model ( $\mathcal{H}_0$ ) is also shown. It is seen that this is considerably less successful in predicting the observed angular dependence.

The implications of these comparisons with experimental data will be further discussed in the next section.

## 6. Discussion

### 6.1. Inertial instabilities and the critical Reynolds number

It should now be clear that the classical lubrication approximation with the assumption of  $\epsilon Re \ll 1$  is insufficient for predicting the loss of stability in vertical/inclined film boiling, and by extension, that it is insufficient for predicting the heat transfer coefficient. As shown in Sec. 2.3.2, the approximation is not self-consistent. Additionally, as seen in Sec. 3.4, the approximation yields a dispersion relation that has no significant mechanism for instability in the vertical case, which would incorrectly predict a vapor film that remains smooth indefinitely. Note that this does not discredit the  $\epsilon Re \ll 1$  approximations made in works such as Panzarella et al. (2000); Aursand et al. (2018), since those are concerned with horizontal film-boiling with no strong buoyancy-induced net vapor-flow.

By retaining the inertial terms and using an integral method, it is possible to derive a valid long-wave model.

Linear stability analysis of said model results in a dispersion relation, Eq. (55), that reveals neutral curves such as Fig. 4 and by extension predicted values for the critical Reynolds number and wavenumber. Characterizing film boiling stability through a critical Reynolds number has been suggested before by authors such as Kim and Suh (2013), though they fitted a value to a combination of HTC and velocity measurements, as opposed to theoretically predicting it. As seen in Fig. 4, in the present work a value of  $Re_c \approx 10$  is predicted for water. This theoretical prediction is consistent with the experimental findings of Kim and Suh (2013).

As shown in Sec. 3.5, for the vertical case the predicted critical Reynolds number and wavenumber for any case may to a good approximation be represented by simple power laws with weak dependencies on the parameters  $S$  and  $B$ . The only result of the stability analysis that carries over into the HTC model is the dimensional wavelength of the resulting disturbances, called the critical wavelength  $\lambda_c$ . Since  $Re$  grows very fast as the film thickness grows ( $\sim h_0^3$ ),  $\lambda_c$  depends only weakly on the critical Reynolds number, as seen in Eq. (65) ( $\sim Re_c^{1/3}$ ). As seen in Eq. (67), the overall result for the vertical case is that this wavelength is only weakly dependent on  $S$  and  $B$  and that it is accurately predicted by the fluid-dependent wavelength  $\lambda_0$  multiplied with a relatively constant ( $\approx 100$ ) factor.

### 6.2. Validity of the model and its approximations

While inertial terms were retained, the present long-wave approximation still assumes that the  $\mathcal{O}(\epsilon^2)$  terms could be neglected, and it is necessary for self-consistency

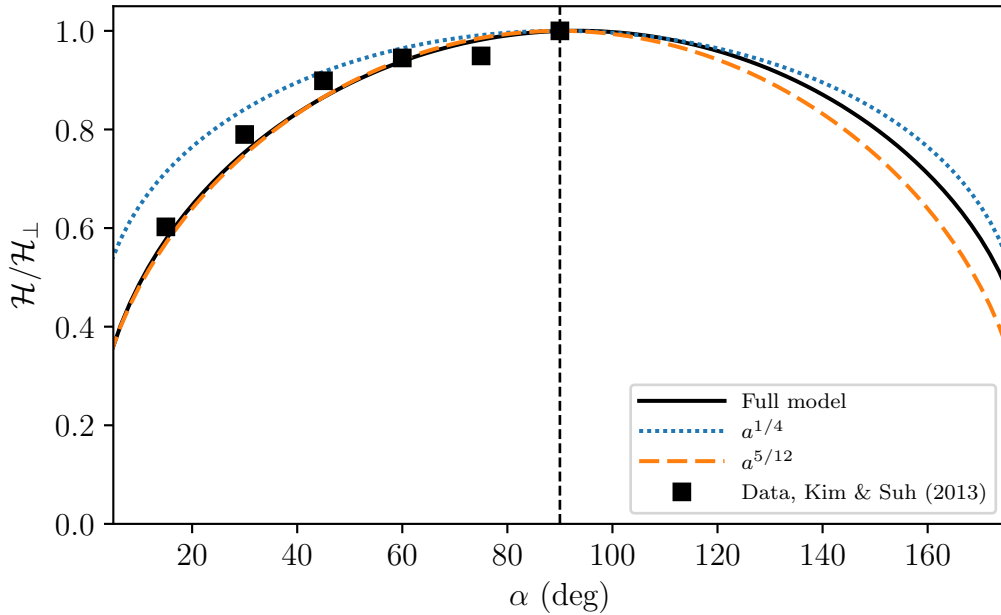


Figure 8: Experimentally measured heat transfer coefficients for water with  $\Delta T = 150$  K at varying inclination angles, relative to the value in the vertical orientation. The solid line shows the prediction of the present model. The dashed line shows the approximation resulting from Eq. (72) ( $a^{5/12}$ ). The dotted line shows the angular dependence of the Bromley-type models ( $a^{1/4}$ ).

that the predicted instabilities from the model have wavelengths that satisfy this assumption. According to the definitions in Sec. 3.2, the condition of  $\epsilon \ll 1$  is equivalent to  $k \ll 1$ . As seen from Fig. 4 and Eq. (64), the first occurring instability generally has  $k \sim 0.1$  in the vertical cases, and for other orientations  $k$  is smaller. Thus, the  $\mathcal{O}(\epsilon^2)$  terms may safely be neglected compared to the  $\mathcal{O}(1)$  terms.

Additionally, in order to simplify the model, it was assumed in Sec. 2.4.3 that  $E \ll 1$ . Since the value of  $E$  becomes smaller as the vapor film grows thicker, self-consistency would require that the predicted onset of instabilities occurs after  $E$  becomes small. The value of  $E$  along the growing base state is  $E(x) = S/\text{Re}(x)$ . Since  $S \sim 0.1$  and  $\text{Re}_c \sim 10$ , one can expect that  $E \sim 0.01$  by the time instabilities occur, which is certainly small enough to make the approximation reasonable.

### 6.3. Heat-transfer coefficient

In order to predict the heat-transfer coefficient, the premise of the LVFU model was accepted at face value, and the only result needed from the model herein was the critical wavelength  $\lambda_c$  in Eq. (65) inserted into Eq. (2). The result was the general expression, Eq. (68), where the critical wavelength's dependence on  $\lambda_0$  carried over into the reference HTC ( $\mathcal{H}_0$ ), while the relatively weak dependence on  $S/B^2$  carried over into the corresponding Nusselt number.

As seen in Fig. 6, the present model appears to work very well for vertical film boiling. It is interesting to note how most of the variation in the HTC between different fluids and  $\Delta T$  values is accounted for by  $\mathcal{H}_0$  alone. Such a

constant-Nu model, seen in the dotted line in Fig. 6, seems quite sufficient for small to moderate superheat ( $\Delta T/T_s < 1$ ). This means that the wavelength  $\lambda_0$  combined with the LVFU model is a good predictor for the HTC and that variations in the Nusselt number, as defined here, only accounts for a moderate adjustment. This is confirmed experimentally in Fig. 7 by the fact that every single measurement shows approximately the same Nusselt number,

$$\text{Nu}_\perp \approx 0.4 \pm 0.1, \quad (73)$$

regardless of fluid and  $\Delta T$ . For the little variation in Nu there is, Fig. 7 shows that the predicted weak power-law  $(S/B^2)^{1/24}$  fits quite well.

The reason for the almost universal Nusselt number,  $\text{Nu} \approx 0.4$ , seems to be due to the fact that the critical Reynolds number  $\text{Re}_c$  and the corresponding dimensionless wavenumber  $k_c$  vary little from case to case, as seen from the weak  $S$  and  $B$  power-laws in Eqs. (63) and (64). This leads to the critical wavelength in Eq. (67) having a weak dependence on  $S$  and  $B$  and essentially being just  $\lambda_0$  times a slightly varying factor. Since the dependence on  $\lambda_0$  is absorbed into the definition of  $\mathcal{H}_0$ , the Nusselt number is left to only account for a small adjustment.

For the vertical case, it is apparent from Fig. 6 that the difference between the full model and the approximation in Eq. (71) is virtually zero, so there is little reason to not use the latter. In the case of general inclination, one must either solve the full stability problem, or combine Eq. (71) with the approximation Eq. (72). As seen in Fig. 8, the two give practically identical results in the cases where  $\alpha \leq \pi/2$ . It is also apparent from Fig. 8 that the classical

inclination dependence of  $a^{1/4}$  from LSI-type models are less accurate at predicting the observations. Overall there is too little data to draw strong conclusions regarding the inclination dependence. In the  $\alpha > \pi/2$  configurations, there seems to be no data at all, and it is not even clear if LVFU-type models apply at all due to the possibility of bubble detachment.

## 7. Conclusions

From the present work the following may be concluded:

- Retaining the inertial ( $\epsilon\text{Re}$ ) terms in the long-wave approximation is crucial for correctly predicting stability in non-horizontal film boiling.
- When applying an integral boundary layer method to the long-wave approximation with inertial terms, the result is the two coupled nonlinear partial differential equations in Eqs. (46) and (47).
- Linear stability analysis of this model indicates that the critical Reynolds number for the onset of the inertial instabilities is  $\text{Re}_c \approx 10$  and that the resulting waves are much longer than the film thickness.
- Before the critical Reynolds number is reached, the stabilizing evaporation effect seems to dominate. After it is reached, the film is so thick that vapor thrust, non-equilibrium and thermocapillary effects are negligible.
- For inclination angles  $\alpha \leq \pi/2$ , as defined in Fig. 1, the present model implies that the long-plate film-boiling heat-transfer coefficient may be quite accurately predicted by

$$\mathcal{H} = 0.901 (\sin \alpha)^{5/12} \left( \frac{S}{B^2} \right)^{1/24} \left( \frac{\xi k_v^3 \rho_v \Delta \rho g \hat{L}}{16 \mu_v \Delta T \lambda_0} \right)^{1/4}, \quad (74)$$

with  $S$  and  $B$  given by Eqs. (5) and (62), and the vapor properties evaluated at the film-temperature. This model could predict all relevant heat transfer coefficient data within an error of 15%. The model is non-empirical, in the sense that the pre-factor 0.9010 comes from expressions generated by numerical solutions of  $\text{Re}_c$  and  $k_c$ , and not from experimental data.

The full nonlinear model Eqs. (46) and (47), and the subsequent results derived thereof, are all made under the assumption of  $E \ll 1$ , which implies that the vapor film thickness  $\bar{h}(x)$  has grown to be at least 100  $\mu\text{m}$  and is quite parallel to the solid wall. As possible further work, it would be interesting to explore the properties of vapor film stability in the regime where  $E \approx 1$ . This could involve either solving the full nonlinear model numerically, or performing some nonparallel stability analysis akin to Saric and Nayfeh (1975).

## Acknowledgements

E. Aursand was supported by the Research Council of Norway [244076/O80] and The Gas Technology Centre (NTNU–SINTEF) through the funding program MAROFF. His research visit at Northwestern University was supported by the U.S.-Norway Fulbright Foundation. Thanks to Bernhard Müller, Tor Ytrehus, Svend Tollak Munkejord, and Morten Hammer for discussions and feedback. Finally, thanks to Hunter Beck for language assistance.

## References

- S. V. Alekseenko, V. E. Nakoryakov, and B. G. Pokusaev. Wave formation on vertical falling liquid films. *International journal of multiphase flow*, 11(5):607–627, 1985. doi: 10.1016/0301-9322(85)90082-5.
- E. Aursand. Inclination dependence of planar film boiling stability. *International Journal of Multiphase Flow*, 106:243–253, 2018. doi: 10.1016/j.ijmultiphaseflow.2018.05.010.
- E. Aursand, S. H. Davis, and T. Ytrehus. Thermocapillary instability as a mechanism for film boiling collapse. *Journal of Fluid Mechanics*, 852:283–312, 2018. doi: 10.1017/jfm.2018.545.
- L. A. Bromley. Heat transfer in stable film boiling. *Chemical Engineering Progress*, 46:221–227, 1950.
- T. D. Bui and V. K. Dhir. Film boiling heat transfer on an isothermal vertical surface. *ASME J. Heat Transfer*, 107(4):764–771, 1985. doi: 10.1115/1.3247502.
- J. P. Burelbach, S. G. Bankoff, and S. H. Davis. Nonlinear stability of evaporating/condensing liquid films. *Journal of Fluid Mechanics*, 195:463–494, 1988. doi: 10.1017/S0022112088002484.
- H. Chang. Wave evolution on a falling film. *Annual review of fluid mechanics*, 26(1):103–136, 1994. doi: 10.1146/annurev.fl.26.010194.000535.
- R. V. Craster and O. K. Matar. Dynamics and stability of thin liquid films. *Reviews of modern physics*, 81(3):1131–1198, 2009. doi: 10.1103/RevModPhys.81.1131.
- S. H. Davis. Thermocapillary instabilities. *Annual Review of Fluid Mechanics*, 19(1):403–435, 1987. doi: 10.1146/annurev.fl.19.010187.002155.
- V. K. Dhir. Boiling heat transfer. *Annual review of fluid mechanics*, 30(1):365–401, 1998. doi: 10.1146/annurev.fluid.30.1.365.
- Y.-Y. Hsu and J. W. Westwater. Film boiling from vertical tubes. *AIChE Journal*, 4(1):58–62, 1958. doi: 10.1002/aic.690040112.
- S. W. Joo, S. H. Davis, and S. G. Bankoff. Long-wave instabilities of heated falling films: two-dimensional theory of uniform layers. *Journal of Fluid Mechanics*, 230:117–146, 1991. doi: 10.1017/S0022112091000733.
- N. Kaneyasu and I. Takehiro. Two-phase boundary-layer treatment of free-convection film boiling. *International Journal of Heat and Mass Transfer*, 9(2):103–115, 1966. doi: 10.1016/0017-9310(66)90125-6.
- C. S. Kim and K. Y. Suh. Angular dependency on film boiling heat transfer from relatively long inclined flat plates. *Journal of Heat Transfer*, 135(12):121502, 2013. doi: 10.1115/1.4024583.
- J. C. Y. Koh. Analysis of film boiling on vertical surfaces. *Journal of Heat Transfer*, 84(1):55–62, 1962. doi: 10.1115/1.3684293.
- N. I. Kolev. Film boiling on vertical plates and spheres. *Experimental Thermal and Fluid Science*, 18(2):97–115, 1998. doi: 10.1016/S0894-1777(98)10021-3.
- P. K. Kundu, I. M. Cohen, and D. R. Dowling. *Fluid Mechanics*. Academic Press, Cambridge, 5th edition, 2007. ISBN 9780123821003.
- S.-P. Liaw and V. K. Dhir. Effect of surface wettability on transition boiling heat transfer from a vertical surface. In *Proceedings of the 8th international heat transfer conference*, volume 4, pages 2031–2036, 1986.
- T. G. Myers. Thin films with high surface tension. *SIAM Review*, 40(3):441–462, 1998. doi: 10.1137/S003614459529284X.

- S. Nishio and G. R. Chandratilleke. Steady-state pool boiling heat transfer to saturated liquid helium at atmospheric pressure. *JSME international journal. Ser. 2, Fluids engineering, heat transfer, power, combustion, thermophysical properties*, 32(4):639–645, 1989. doi: 10.1299/jsmeb1988.32.4\_639.
- S. Nishio and G. R. Chandratilleke. Natural-convection film-boiling heat transfer: Saturated film boiling with long vapor film. *JSME international journal. Ser. 2, Fluids engineering, heat transfer, power, combustion, thermophysical properties*, 34(2):202–211, 1991. doi: 10.1299/jsmeb1988.34.2\_202.
- S. Nishio and H. Ohtake. Vapor-film-unit model and heat transfer correlation for natural-convection film boiling with wave motion under subcooled conditions. *International journal of heat and mass transfer*, 36(10):2541–2552, 1993. doi: 10.1016/S0017-9310(05)80192-9.
- S. Nukiyama. The maximum and minimum values of the heat Q transmitted from metal to boiling water under atmospheric pressure. *Journal of Japan Society of Mechanical Engineers*, 37:367–374, 1934.
- T. Okkonen, H. Wennerstroem, S. Hedberg, J. Blomstrand, B.R. Sehgal, and W. Frid. Film boiling on a long vertical surface under high heat flux and water subcooling conditions. In *AICHE symposium series*, volume 92, pages 294–303. American Institute of Chemical Engineers, 1996.
- A. Oron, S. H. Davis, and S. G. Bankoff. Long-scale evolution of thin liquid films. *Reviews of modern physics*, 69(3):931–980, 1997. doi: 10.1103/RevModPhys.69.931.
- C. H. Panzarella, S. H. Davis, and S. G. Bankoff. Nonlinear dynamics in horizontal film boiling. *Journal of Fluid Mechanics*, 402:163–194, 2000. doi: 10.1017/S0022112099006801.
- T. Prokopiou, M. Cheng, and H.-C. Chang. Long waves on inclined films at high reynolds number. *Journal of fluid mechanics*, 222:665–691, 1991. doi: 10.1017/S002211209100126X.
- W. S. Saric and A. H. Nayfeh. Nonparallel stability of boundary-layer flows. *The Physics of Fluids*, 18(8):945–950, 1975. doi: 10.1063/1.861266.
- N. V. Suryanarayana and H. Merte. Film boiling on vertical surfaces. *Journal of Heat Transfer*, 94(4):377–384, 1972. doi: 10.1115/1.3449955.
- R. Vijaykumar and V. K. Dhir. An experimental study of subcooled film boiling on a vertical surface—thermal aspects. *Journal of heat transfer*, 114(1):169–178, 1992. doi: 10.1115/1.2911243.

## Appendix A. Derivation of dimensionless equations

The following derivation is similar to the one in [Aursand et al. \(2018\)](#) for horizontal film boiling, but generalized for any orientation. Readers are directed there for more detailed comments on the model assumptions that do not relate to the generalization.

### Appendix A.1. Governing equations

The two-dimensional vapor flow in Fig. 1 is characterized by a velocity field  $\mathbf{v} = u\hat{\mathbf{x}} + w\hat{\mathbf{z}}$ , a temperature field  $T$ , and a pressure field  $p$ . The governing equations are the standard continuity equation,  $x$  and  $z$  momentum equations, and the energy equation ([Kundu et al., 2007](#)),

$$u_x + w_z = 0, \quad (\text{A.1})$$

$$\rho_v (u_t + uu_x + ww_z) = -p_x + \mu_v (u_{xx} + u_{zz}) - \phi_x, \quad (\text{A.2})$$

$$\rho_v (w_t + uw_x + ww_z) = -p_z + \mu_v (w_{xx} + w_{zz}) - \phi_z, \quad (\text{A.3})$$

$$\rho_v c_{p,v} (T_t + uT_x + wT_z) = k_v (T_{xx} + T_{zz}), \quad (\text{A.4})$$

where subscripts  $t$ ,  $x$  and  $z$  imply differentiation. The body-force potential  $\phi$ ,

$$\phi = \phi_0 + \rho_v g (ax + bz) + \frac{\tilde{A}}{6\pi h^3(x)}, \quad (\text{A.5})$$

includes not only the gravitational potential, but also a *disjoining pressure* term ([Oron et al., 1997](#)) that represents the van der Waals interaction. Here  $\phi_0$  is a constant reference potential,  $g$  is the gravitational acceleration,  $\tilde{A}$  is the Hamaker constant. The quantities  $a$  and  $b$  are the inclination dependent shorthands  $a = \sin(\alpha)$  and  $b = -\cos(\alpha)$ .

### Appendix A.2. Boundary conditions

At the solid wall we have zero velocity and a given temperature  $T_w$ ,

$$[\mathbf{v}]_{z=0} = 0, \quad (\text{A.6})$$

$$[T]_{z=0} = T_w. \quad (\text{A.7})$$

At the liquid–vapor interface  $z = h(x, t)$  the boundary conditions are continuity of tangential velocity, the kinematic boundary condition (with evaporation), the normal stress balance, the tangential stress balance, and the energy balance. In this order, these may be formally written as

$$[(\mathbf{v} - \mathbf{v}_1) \cdot \hat{\mathbf{t}}]_{z=h} = 0, \quad (\text{A.8})$$

$$\rho_v [(\mathbf{v}_1 - \mathbf{v}) \cdot \hat{\mathbf{n}}]_{z=h} = j \quad (\text{A.9})$$

$$[j(\mathbf{v}_1 - \mathbf{v}) \cdot \hat{\mathbf{n}} - ([\mathcal{T} - \mathcal{T}_1] \cdot \hat{\mathbf{n}}) \cdot \hat{\mathbf{n}}]_{z=h} = -\kappa\sigma \quad (\text{A.10})$$

$$[[([\mathcal{T} - \mathcal{T}_1] \cdot \hat{\mathbf{n}}) \cdot \hat{\mathbf{t}} - \nabla\sigma \cdot \hat{\mathbf{t}}]_{z=h} = 0 \quad (\text{A.11})$$

$$-k_v [\nabla T \cdot \hat{\mathbf{n}}]_{z=h} = \mathcal{H}_1 (T_i - T_s) + j\hat{L}. \quad (\text{A.12})$$

Here a subscript “1” indicates the corresponding property on the liquid side of the interface. The symbol  $\mathcal{T}$  is the Newtonian flow viscous stress tensor,  $j$  is the evaporation mass flux, and  $\hat{L}$  is the effective latent heat of vaporization (modified for the sensible heat effect according to [Bui and Dhir \(1985\)](#)). The interface has unit vectors  $\hat{\mathbf{n}}$  and  $\hat{\mathbf{t}}$  defined according to Fig. 1, a velocity given by  $\mathbf{v}_1$ , and a temperature  $T_i = T(x, z = h)$  which during evaporation is slightly higher than the saturation (and liquid bulk) temperature  $T_s$ . The heat transfer coefficient between the interface and the liquid bulk is  $\mathcal{H}_1$ . The surface tension of the interface,  $\sigma$ , depends on the interface temperature. This dependence is approximated as a linearization around a value  $\sigma_0$  at  $T_s$  ([Davis, 1987](#)),

$$\sigma(T) = \sigma_0 - \gamma [T - T_s]. \quad (\text{A.13})$$

As discussed in [Aursand et al. \(2018\)](#) the evaporation mass flux may be modelled according to kinetic theory,

$$T_i - T_s = \tilde{K}j, \quad (\text{A.14})$$

with

$$\tilde{K} = \left( \frac{1 - \frac{1}{2}\alpha_e}{\alpha_e} \right) \frac{\sqrt{2\pi} R_s T_s^{3/2}}{\rho_v L}, \quad (\text{A.15})$$

where  $\alpha_e$  is the evaporation coefficient with an assumed value of 0.85.

Finally, in order to avoid having to compute the detailed dynamics of the bulk liquid outside the vapor film, some additional simplifying assumptions are made. First, it is assumed that the liquid pressure is given by hydrostatics alone, so that the liquid pressure  $p_l$  outside the interface is

$$[p_l]_{z=h} = -\rho_l g(ax + bh). \quad (\text{A.16})$$

Second, it is assumed that the tangential interface velocity must be somewhere between zero and the hypothetical maximum (free surface,  $\mu_l \rightarrow 0$ ),

$$[\mathbf{v} \cdot \hat{\mathbf{t}}]_{z=h} = \eta \left( \lim_{\mu_l \rightarrow 0} [\mathbf{v} \cdot \hat{\mathbf{t}}]_{z=h} \right) \quad (\text{A.17})$$

with the fluid-dependent constant  $\eta \in (0, 1)$  specifying the position within this range.

### Appendix A.3. Scales and dimensionless numbers

As commonly done in the long-wave approximation, a film thickness scale  $h_0$  is used to define dimensionless equivalents  $Z = z/h_0$  and  $H = h/h_0$ . The dimensionless parallel distance is scaled according to the wavelength  $\lambda$  of the vapor film disturbances,  $X = x/x_0$  with  $x_0 = \lambda/(2\pi)$ . The aspect ratio central to this approximation is simply the ratio between these two scales,  $\epsilon = h_0/x_0$ . For the velocity components a scale  $u_0$  is used to define dimensionless equivalents  $U = u/u_0$  and  $W = w/w_0$ , where continuity implies that  $w_0 = \epsilon u_0$ . Time is scaled according to  $t_0 = x_0/u_0$ , which is used to define the dimensionless time  $\tau$ . The dimensionless pressure  $P$  and potential  $\Phi$  are defined using the pressure scale implied by viscous pressure-drop in a channel,  $p_0 = \mu_v u_0 / (\epsilon h_0)$ . The evaporation rate  $J = j/j_0$  is scaled with  $j_0 = k_v \Delta T / (h_0 L)$ , where  $\Delta T = T_w - T_s$ . Finally, the dimensionless temperature is  $\theta = (T - T_s) / \Delta T$ .

Without any further knowledge about the velocity scale  $u_0$ , the dimensionless numbers listed in Sec. 2.2.1 may now

generally be written as

$$\begin{aligned} \text{Re} &= \frac{\rho_v u_0 h_0}{\mu_v} && (\text{Reynolds number}), \\ E &= \frac{k_v \Delta T}{\rho_v u_0 h_0 L} && (\text{Evaporation number}), \\ \text{Ca} &= \frac{\mu_v u_0}{\sigma_0} && (\text{Capillary number}), \\ K &= \frac{\tilde{K} k_v}{h_0 \hat{L}} && (\text{Disequilibrium number}), \\ M &= \frac{\Delta T \gamma}{\mu_v u_0} && (\text{Marangoni number}), \\ S &= \frac{k_v \Delta T}{\mu_v \hat{L}} && (\text{Vapor-thrust number}), \\ \text{Pr} &= \frac{\mu_v c_{p,v}}{k_v} && (\text{Vapor Prandtl number}), \\ \Psi &= \mu_v / \mu_l && (\text{Viscosity ratio}), \\ G_v &= \frac{\rho_v g h_0^2}{\mu_v u_0} && (\text{Vapor gravity number}), \\ G_l &= \frac{\rho_l g h_0^2}{\mu_v u_0} && (\text{Liquid gravity number}), \\ G &= \frac{\Delta \rho g h_0^2}{\mu_v u_0} && (\text{Gravity number}). \end{aligned} \quad (\text{A.18})$$

The dimensionless governing equations and boundary conditions listed in Sec. 2.2.1 result from combining the governing equations of Appendix A.1 and the boundary conditions of Appendix A.2 with the dimensionless scalings and numbers herein. In this process, the effects of van der Waals interactions in Eq. (A.5) and liquid heat transfer in Eq. (A.12) are neglected.

## Appendix B. Base state velocity profile

According to total mass conservation, a steady state solution must have the same rate of vapor flowing out at  $x$  as the rate of vapor that is supplied through evaporation along the entire length of  $0 \rightarrow x$ . This means that the average vapor velocity corresponding to the simplified steady state in Eq. (32) may be written as a function of the growing film thickness,

$$\begin{aligned} \langle \bar{u} \rangle &= \frac{1}{\rho_v \bar{h}} \int_0^x \frac{k_v \Delta T}{\hat{L} \bar{h}(x')} dx', \\ &= \frac{a \xi \Delta \rho g \bar{h}^2}{12 \mu_v}. \end{aligned} \quad (\text{B.1})$$

The special case of Eq. (B.1) with  $a = 0$  and  $\xi = 1$  is what inspired the choice of velocity scale  $u_0$  in Eq. (4). With this scaling the dimensionless velocity profile of the base state is

$$\bar{U} = \frac{Ga}{2} [(1 + \eta) \bar{H} Z - Z^2], \quad (\text{B.2})$$

which means that the interface velocity and maximum velocity are

$$\bar{U}_i = \frac{Ga}{2} \eta \bar{H}^2, \quad \bar{U}_{\max} = \frac{Ga}{2} \left[ \frac{1}{4} (1 + \eta)^2 \right] \bar{H}^2, \quad (\text{B.3})$$

respectively.

### Appendix C. The value of $\eta$

As seen from Eq. (B.3), information on the velocity profile in film boiling may give insight into what the value of  $\eta$  should be. From the theoretical calculations by Koh (1962) on the velocity profile in smooth steady solutions one can see that

$$\frac{U_i}{U_{\max}} \approx \frac{3}{4} \left( \frac{\rho_v \mu_v}{\rho_l \mu_l} \right)^{1/4}. \quad (\text{C.1})$$

Since Eq. (B.3) implies that

$$\frac{\bar{U}_i}{\bar{U}_{\max}} = 4 \frac{\eta}{(1 + \eta)^2} \approx 4\eta, \quad (\text{C.2})$$

the value of  $\eta$  may then be approximated by

$$\eta \approx \frac{1}{4} \frac{U_{\max}}{U_i} \approx \frac{3}{16} \left( \frac{\rho_v \mu_v}{\rho_l \mu_l} \right)^{1/4}. \quad (\text{C.3})$$